Electronic and optical properties of nonpolar *a*-plane GaN quantum wells

S. Schulz,[1] T. J. Badcock,[2] M. A. Moram,[3] P. Dawson,[2] M. J. Kappers,[3] C. J. Humphreys,[3] and E. P. O'Reilly[1,4]
[1]*Photonics Theory Group, Tyndall National Institute, Lee Maltings, Cork, Ireland*
[2]*School of Physics and Astronomy, Photon Science Institute, University of Manchester, Alan Turing Building, Manchester M13 9PL, United Kingdom*
[3]*Department of Materials Science & Metallurgy, University of Cambridge, Pembroke Street, Cambridge CB2 3QZ, United Kingom*
[4]*Department of Physics, University College Cork, Cork, Ireland*
(Received 6 May 2010; revised manuscript received 13 August 2010; published 16 September 2010)

In this paper we present a detailed study of the electronic band structure of a series of nonpolar *a*-plane GaN/AlGaN multiple quantum wells (QWs) of varying well width using complementary results from x-ray diffraction, polarization-dependent photoluminescence excitation spectroscopy, and $\mathbf{k}\cdot\mathbf{p}$ theory. When excited with unpolarized light, excitonic transitions involving different electron subbands are resolved in the excitation spectra. For linearly polarized ($E\perp c, E\parallel c$) excitation, these are shown to consist of overlapping transitions involving different hole subbands. These results are then analyzed in detail using strain data determined by the x-ray diffraction measurements in combination with the $\mathbf{k}\cdot\mathbf{p}$ theory to calculate the bulk band structure and the relative oscillator strength of an *a*-plane GaN film under strain. The results are compared with those of an unstrained *c*-plane film. This analysis reveals that the experimentally observed polarization anisotropy can be attributed to anisotropic strain in the *c* plane. Based on the $\mathbf{k}\cdot\mathbf{p}$ Hamiltonian, we apply an effective mass approximation, taking into account strain and nonparabolicity effects, to calculate the single-particle states and energies for the different quantum wells. The possible influence of the weak spin-orbit coupling on the results is studied in detail. Starting from the single-particle energies and including excitonic binding energies, the band edge optical transitions are calculated and successfully compared to the experimental data. Our analysis gives an estimate for the conduction- to valence-band offset ratio of 45:55 for nonpolar GaN/AlGaN QW structures. Additionally, our study also allows us to investigate the magnitude of the crystal-field splitting and spin-orbit coupling in GaN systems.

DOI: 10.1103/PhysRevB.82.125318 PACS number(s): 73.21.Fg, 71.35.−y, 71.70.Fk, 78.67.De

I. INTRODUCTION

The rapid progress in the growth of nitride semiconductors has enabled the development of high power/temperature optoelectronic devices.[1] Since the zinc-blende crystal phase of group-III nitrides is metastable,[2] the vast majority of current state-of-the-art nitride-based optoelectronic devices utilize *c*-plane wurtzite heterostructures, even though the performance of these devices suffers from strong electrostatic built-in fields arising from the growth along the *c* direction.[3,4] As a consequence of the quantum confined Stark effect, the oscillator strength of the radiative transitions is strongly reduced and is accompanied by a redshift of the emission.[5] To overcome these problems associated with growth along the *c* axis, the growth of low-dimensional systems along nonpolar directions (e.g., *a*- and *m*-plane directions) has been proposed.[6,7] From a theoretical point of view the elimination of the built-in field in nonpolar quantum wells (QWs) is obvious since the heterostructure has no facets along the *c* direction.[8] In recent years, several groups have experimentally confirmed the absence of polarization fields in nonpolar nitride-based heterostructures. Waltereit *et al.*[6] first successfully demonstrated polarization-field-free *m*-plane GaN/AlGaN multiple QWs in 2000. Driven by the progress in the epitaxial growth techniques, high performance *m*-plane light emitting devices,[9] *m*-plane violet laser diodes,[10] and *m*-plane blue laser diodes[11] have been reported. In addition to the benefits of the absence of the electrostatic built-in fields in nonpolar nitride-based QWs, the change in crystal symmetry from wurtzite to orthorhombic in nonpolar GaN films has been demonstrated to induce in-plane optical polarization anisotropy,[12] a characteristic potentially useful in polarization sensitive devices.[7] Therefore, a detailed characterization of these structures both theoretically and experimentally is of great interest.

To the best of our knowledge, a comprehensive analysis of structural measurements and optical investigations in combination with electronic-structure calculations has been restricted to nonpolar GaN nitride films.[13–16] In this paper we present a detailed investigation of a series of nonpolar *a*-plane GaN/AlGaN QWs, grown on *r*-plane sapphire, of varying QW width using results from x-ray diffraction (XRD), polarization-dependent photoluminescence excitation (PLE) spectroscopy, and $\mathbf{k}\cdot\mathbf{p}$ theory, to analyze the material properties.

The structures studied contained ten periods of $GaN/Al_{0.18}Ga_{0.82}N$ QWs deposited on 5 μm thick *a*-plane GaN templates on *r*-plane sapphire substrates. The samples were grown in a 6×2 inch Thomas Swan metal organic vapor-phase epitaxy close-coupled showerhead reactor. Five QW samples were grown, containing GaN QWs of thicknesses ranging from 24 to 72 Å in the different samples, with each containing 108 Å thick $Al_{0.18}Ga_{0.82}N$ barriers. Further details of the growth and structural characterization of the samples are published elsewhere.[17]

To begin with we apply XRD measurements to determine the strain state of the system. For nonpolar *a*-plane GaN grown on *r*-plane sapphire, there is considerable in-plane anisotropy in the lattice parameters, thermal expansion coeffi-

cients, and elastic constants of both the GaN film and the sapphire substrate. This will lead to an in-plane anisotropic strain in the GaN epilayer, which is expected to affect the optical properties of the films. In addition, a wide range of "unstrained" GaN reference lattice parameters are reported in the literature,[18] attributable to variations in the impurity and electronic doping levels produced by different film growth conditions. There is also considerable uncertainty in the thermal expansion coefficients and elastic constants of the III nitrides[18] since high densities of defects are typically present in nonpolar GaN. As a result, the strain state of the nonpolar GaN film cannot be predicted accurately, so experimental determination of the strain state is required.

Using the measured strain data, we then perform $\mathbf{k}\cdot\mathbf{p}$-based electronic-structure calculations of nonpolar *a*-plane GaN/AlGaN QWs as a function of the QW width. To achieve a detailed analysis of the differences between polar and nonpolar systems we start with the investigation of the band structure of *c*- and *a*-plane systems under strain and compare the results. We also study the relative oscillator strength along orthogonal directions of the lowest energy interband transition at the Brillouin-zone center in *c*-plane and *a*-plane GaN as a function of the in-plane strain. These results are then compared to PL data acquired from the bulk *a*-plane GaN template characterized previously by XRD. The observed polarization anisotropy is very different from the polarization isotropy observed in "conventional" *c*-plane systems. After this discussion of the bulk system we will turn our attention to the electronic structure of the *a*-plane $GaN/Al_{0.18}Ga_{0.82}N$ QWs. Our analysis reveals that the optical properties of these structures are determined by the wavefunction character of the highest valence-band (VB) states, which are made predominately of *p* states oriented in the growth plane. The QW width dependencies of the single-particle energies are then determined, including the effects of conduction-band nonparabolicity, spin-orbit (SO) coupling, and strain contributions.

We then report on the low-temperature PLE spectroscopy of the nonpolar *a*-plane $GaN/Al_{0.18}Ga_{0.82}N$ multiple QWs. From the PLE data, details of the band structure of the QWs are revealed. Excitation with unpolarized light resulted in the observation of exciton transitions associated with different electron subbands. However, when using linearly polarized excitation ($E\perp c, E\| c$), these transitions were shown to consist of overlapping transitions involving different valence subbands. Allowing for a QW width-dependent exciton binding energy, determined using a fractional dimensional space approach,[19,20] the energies of the band-edge transitions are calculated and successfully compared to the experimental data.

The paper is organized in the following way. Section II is dedicated to the XRD analysis of the strain state for the system under consideration. In Sec. III the electronic-structure calculation is described in detail. Section IV presents the results of the polarized PLE measurements and a comparison with the theoretical predictions. Finally, we conclude with a short summary of the obtained results in Sec. V.

II. X-RAY ANALYSIS

High-resolution XRD (HRXRD) analysis was carried out using a PANalytical X-Pert Pro MRD diffractometer with a mirror, a four-bounce asymmetric Ge(220) monochromator and a triple-bounce analyzer. Cu $K\alpha_1$ radiation of wavelength 1.5405974(15) Å was used.[18] HRXRD reciprocal space maps obtained in the asymmetric geometry were used to characterize the lattice parameters and hence the strain state of the sample. All measurements were performed at room temperature.

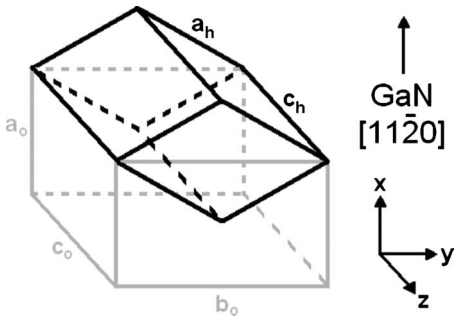

FIG. 1. Illustration of the relative orientation of the unit cells used to describe the crystal structure of nonpolar *a*-plane films. The original hexagonal unit cell is shown in black; the related orthorhombic unit cell is shown in gray. The *y* and *z* axes lie in the plane of the film, with *z* parallel to the wurtzite *c* axis.

In nonpolar GaN films, the presence of anisotropic in-plane strain will produce a distortion of the hexagonal unit cell. As a result, the crystal structure can be described better using an orthorhombic unit cell, in which the *x* axis is perpendicular to the film surface and the *y* and *z* axes lie in the plane of the film, with *z* along the wurtzite *c* axis as illustrated in Fig. 1. This permits the strains in each direction to be quantified conveniently by measuring the departure of the measured orthorhombic lattice parameters from appropriately chosen reference values and by looking at any deviations of the proportions of the unit cell from their ideal values. Suitable reference unstrained hexagonal lattice parameter values and unit-cell proportions were determined from *c*-plane GaN grown in the same metal-organic vapor-phase epitaxy reactor.[21] The reference lattice parameters used were $a_h=3.1884\pm0.0002$ Å and $c_h=5.1850\pm0.0002$ Å and the reference c/a ratio used was 1.6265 ± 0.0002. The corresponding reference lattice parameters of the orthorhombic unit cell illustrated in Fig. 1 were $a_o=3.1884\pm0.0002$ Å, $b_o=5.5225\pm0.0002$ Å, and $c_o=5.1850\pm0.0002$ Å, leading to a reference b/a ratio of 1.7321 ± 0.0002, a reference c/a ratio of 1.6262 ± 0.0002, and a reference c/b ratio of 0.9389 ± 0.0002.

In order to achieve the greatest precision and accuracy in determining the strain state of the nonpolar GaN film, errors in the lattice parameter measurement needed to be minimized. This required investigation of geometrically accessible reflections occurring at high 2θ angles, which also had relatively narrow and intense diffraction peaks, allowing the greatest precision in locating the peak maximum. The presence of crystalline defects (such as basal plane stacking faults and partial dislocations) caused peak broadening; however in some cases it was possible to select reflections which are not broadened by a particular type of defect or to collect reciprocal space maps in a geometry where the reflection is not broadened so strongly.[22] The hexagonal 220, 300, and

302 reflections (occurring at 2θ angles in the region of 149.8°, 113.5°, and 125.2°, respectively) were selected for lattice parameter measurements as they represented the best compromise between these requirements and also helped to minimize cumulative errors in lattice parameter calculations. These reflections could alternatively be indexed as −400, −330, and −332 with respect to the orthorhombic unit cell illustrated in Fig. 1. Where possible, multiple equivalent reflections were measured to assess the reproducibility of the measurement for error analysis purposes. The 2θ values obtained from the asymmetric reciprocal space maps were also corrected for refraction effects;[18] however, the peak width was found to be the main source of error. More accurate lattice parameter measurements could be made for samples with lower defect densities. The resulting lattice parameters of the orthorhombic unit cell were $a_o=3.1914\pm0.0002$ Å, $b_o=5.5170\pm0.0002$ Å, and $c_o=5.1826\pm0.0003$ Å, with lattice parameter ratios of $b/a=1.7287\pm0.0003$, $c/a=1.6239\pm0.0003$, and $c/b=0.9394\pm0.0002$. These measurements confirm a significant departure from the hexagonal symmetry expected of the GaN unit cell. With reference to the orthorhombic unit cell defined in Fig. 1, there is a high in-plane compressive strain of ~0.1% along the b axis and a significantly lower in-plane compressive strain of ~0.05% along the c axis, accompanied by an out-of-plane tensile strain of ~0.1% along the a axis.

III. THEORY

In this part we outline our approach to calculate the electronic and optical properties of nonpolar a-plane $GaN/Al_{0.18}Ga_{0.82}N$ QWs. In Sec. III A we analyze the strained bulk band structure of wurtzite GaN by means of an $\mathbf{k}\cdot\mathbf{p}$ approach and compare the results for c-plane and a-plane GaN.

Using these results we also calculate the relative oscillator strength of the lowest energy interband transition as a function of the strain and compare this to the optical polarization anisotropy observed in emission. Section III B is dedicated to the calculation of the single-particle states and energies in a-plane $GaN/Al_{0.18}Ga_{0.82}N$ QWs, with special attention paid to the possible influence of the weak spin-orbit coupling in the system.

A. Bulk systems

For a detailed description of the bulk band structure around the Brillouin-zone center, and, in particular, to study the influence of the strain and the growth direction, it is useful to apply a multiband approach such as a $\mathbf{k}\cdot\mathbf{p}$ model,[23] a tight-binding approach,[24] or an empirical pseudopotential ansatz.[25]

In order to investigate the influence of the strain on the valence-band structure, we use the $\mathbf{k}\cdot\mathbf{p}$ Hamiltonian given in Ref. 26, including spin-orbit terms introduced following Refs. 27 and 28. Following Ref. 26 the valence-band Hamiltonian of an axially strained III-V material is expanded using basis states with symmetry:

$$(|X\uparrow\rangle,|Y\uparrow\rangle,|Z\uparrow\rangle,|X\downarrow\rangle,|Y\downarrow\rangle,|Z\downarrow\rangle)^T. \tag{1}$$

The Hamiltonian can then be written in the matrix form

$$H=\begin{pmatrix} M_{11}(\mathbf{k}) & M_{12} \\ -M_{12}^{\dagger} & M_{11}^{\dagger}(\mathbf{k}) \end{pmatrix}, \tag{2}$$

where $M_{11}(\mathbf{k})$ and M_{12} are 3×3 matrices and the dagger denotes complex conjugation. The matrix $M_{11}(\mathbf{k})$ can be decomposed in the following way:

$$M_{11}(\mathbf{k})=H_{\mathrm{kp}}(\mathbf{k})+H_{\mathrm{so}}+H_{\mathrm{str}}. \tag{3}$$

$H_{\mathrm{kp}}(\mathbf{k})$ describes the $\mathbf{k}$ dependence of the different energy bands around the Brillouin-zone center,

$$H_{\mathrm{kp}}=\begin{pmatrix} H_{+} & H_{xy} & H_{xz} \\ H_{xy} & H_{-} & H_{yz} \\ H_{xz} & H_{yz} & H_{zz} \end{pmatrix}, \tag{4}$$

where

$$H_{\pm}=(A_1+A_3)k_z^2+(A_2+A_4)(k_x^2+k_y^2)\pm A_5(k_x^2-k_y^2),$$

$$H_{zz}=-\Delta_{\mathrm{cf}}+(A_1)k_z^2+(A_2)(k_x^2+k_y^2),$$

$$H_{xy}=2A_5k_xk_y,$$

$$H_{iz}=\sqrt{2}A_6k_ik_z.$$

The parameters A_i play a similar role as the Luttinger parameters γ_i in a zinc-blende material and are taken from Ref. 29. The crystal-field splitting energy is given by Δ_{cf}.[30] It is due to the wurtzite crystal structure because the $|Z\rangle$-like valence-band state (oriented along the c axis) sees a different environment compared to the $|X\rangle$- and $|Y\rangle$-like valence-band states.

The spin-orbit splitting is introduced through the matrices H_{so} and M_{12}, with

$$H_{\mathrm{so}}=\frac{\Delta_{\mathrm{so}}}{3}\begin{pmatrix} 0 & -i & 0 \\ i & 0 & 0 \\ 0 & 0 & 0 \end{pmatrix} \tag{5}$$

and

$$M_{12}=\frac{\Delta_{\mathrm{so}}}{3}\begin{pmatrix} 0 & 0 & 1 \\ 0 & 0 & -i \\ -1 & i & 0 \end{pmatrix}, \tag{6}$$

where Δ_{so} is the spin-orbit splitting energy. The strain-dependent part of the Hamiltonian matrix H, Eq. (2), for a system under axial strain is given by H_{str},

$$H_{\mathrm{str}}=\begin{pmatrix} S_x & 0 & 0 \\ 0 & S_y & 0 \\ 0 & 0 & S_z \end{pmatrix}. \tag{7}$$

The different components S_α explicitly read

$$S_x=(D_2+D_4)(\epsilon_{xx}+\epsilon_{yy})+D_5(\epsilon_{xx}-\epsilon_{yy})+(D_1+D_3)\epsilon_{zz}, \tag{8}$$

$$S_y=(D_2+D_4)(\epsilon_{xx}+\epsilon_{yy})-D_5(\epsilon_{xx}-\epsilon_{yy})+(D_1+D_3)\epsilon_{zz}, \tag{9}$$

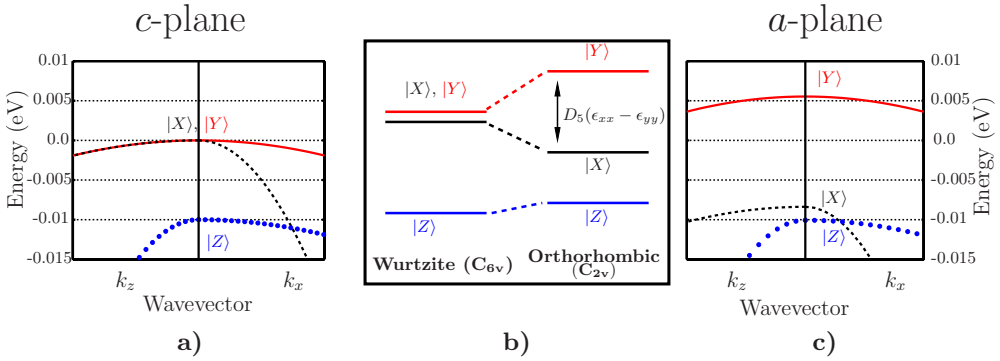

FIG. 2. (Color online) Bulk band structures of (a) *c*-plane and (b) *a*-plane wurtzite GaN; (c) a schematic illustration of the valence-band structure of wurtzite and orthorhombic GaN at $\mathbf{k}=\mathbf{0}$. The growth direction is set along z in the *c*-plane system and along x in the *a*-plane system.

$$S_z = D_2(\epsilon_{xx} + \epsilon_{yy}) + D_1\epsilon_{zz}, \tag{10}$$

where the D_i's denote the valence-band deformation potentials.

To understand the general behavior and the trends in the bulk band structure, initially we neglect the weak spin-orbit coupling in GaN. Doing so, the valence-band structure of the system is described by H_{kp}, Eq. (4), and H_{str}, Eq. (7). For each of the diagonal terms in H_{kp}, the energy dispersion has a light-hole mass along the direction of the given valence-band state and a heavy-hole mass along the orthogonal directions. The valence-band dispersion along the k_x and k_z directions of an unstrained wurtzite *c*-plane bulk GaN system is shown in Fig. 2(a). The energy bands associated with the $|X\rangle$- and $|Z\rangle$-like state have a light-hole mass along the k_x and k_z directions, respectively. The $|Y\rangle$-like state has a heavy mass along all directions in the k_x-k_z plane. The crystal-field splitting Δ_{cf}, shifts the $|Z\rangle$-like valence-band state to lower energy than the $|X\rangle$- and $|Y\rangle$-like states in GaN, as shown in Fig. 2(a).

For a heterostructure grown along the *c* direction (z direction), quantum confinement and strain further split the valence-band states in a compressively strained QW. The first $|Z\rangle$-like state is shifted to lower energies relative to the $|X\rangle$- and $|Y\rangle$-like states. Due to the symmetry of the system in the x-y plane, the strain tensor components ϵ_{xx} and ϵ_{yy} are equal and therefore $S_x=S_y$ in Eq. (7). Furthermore, when looking at Fig. 2(a), the $|X\rangle$- and $|Y\rangle$-like valence-band states have the same effective mass along the k_z direction. From this we can conclude that $|X\rangle$- and $|Y\rangle$-like valence-band states in the absence of the weak spin-orbit coupling generally remain degenerate in a QW heterostructure grown along the *c* direction.

The situation is different in a nonpolar heterostructure, such as an *a*-plane QW system. Here, the strain field is different along all three Cartesian axis directions and therefore the relation $\epsilon_{xx}=\epsilon_{yy}$ is no longer valid. If we assume growth along the x direction, the system exhibits a net tensile strain along this direction ($S_x<0$) and thus the highest $|X\rangle$-like state is shifted to lower energies relative to the energetically highest $|Y\rangle$- and $|Z\rangle$-like states. The splitting between the $|X\rangle$- and $|Y\rangle$-like zone center states is proportional to the term $D_5(\epsilon_{xx}-\epsilon_{yy})$ in S_x and S_y, Eqs. (8) and (9), respectively, as illustrated in Fig. 2(b). A schematic illustration is shown in Fig. 2(c). Due to the positive crystal-field splitting Δ_{cf} in GaN,[31] the highest $|Z\rangle$-like state lies below the highest $|Y\rangle$-like state. Therefore, the ground state in a nonpolar QW or quantum dot (QD) is then dominated by $|Y\rangle$-like states [cf. Figs. 2(b) and 2(c)].

To achieve a more detailed understanding of the polarization properties of the optical transitions in polar and nonpolar nitride-based materials with a wurtzite structure, we next analyze the relative oscillator strength of the lowest energy interband transitions along the x, y, and z directions. These oscillator strengths are directly related to the recombination of electrons in the conduction band with holes in the valence band and therefore to the band structure. Since the strain modifies the band structure of the material and also changes the symmetry of the system, the relative oscillator strength will also be affected. For instance in a nonpolar system, the in-plane strain breaks the symmetry in the basal plane and reduces the symmetry from C_{6v} to C_{2v},[32] hence a strong modification of the interband transition rules is expected.

Therefore, we calculate the relative oscillator strength for *c*-plane and *a*-plane GaN at the Brillouin-zone center ($\mathbf{k}=\mathbf{0}$) as a function of the strain. A similar analysis has been carried out for a GaN *m*-plane system.[14,33] To perform this analysis we start from the full Hamiltonian given in Eq. (2). Here, the ith valence-band wave function is given as a linear combination of $|X\rangle$-, $|Y\rangle$-, and $|Z\rangle$-like states: $|\phi_i^{\mathrm{VB}}\rangle = c_{+,i}^x|X\uparrow\rangle + c_{-,i}^x|X\downarrow\rangle + c_{+,i}^y|Y\uparrow\rangle + c_{-,i}^y|Y\downarrow\rangle + c_{+,i}^z|Z\uparrow\rangle + c_{-,i}^z|Z\downarrow\rangle$. The expansion coefficients $c_{\pm,i}^x$, $c_{\pm,i}^y$, and $c_{\pm,i}^z$ are calculated as functions of the strain from the eigenvectors of the valence-band Hamiltonian H [Eq. (2)]. The optical polarization selection rules are determined by the dipole matrix elements $d_{ij}^2=|\langle\phi_i^{\mathrm{CB}}|\mathbf{e}\cdot\mathbf{p}|\phi_j^{\mathrm{VB}}\rangle|^2$, where $\mathbf{p}$ is the momentum operator and $\mathbf{e}$ the unit vector of the light polarization. The conduction- and valence-band states involved in the transitions are denoted by $|\phi_i^{\mathrm{CB}}\rangle$ and $|\phi_j^{\mathrm{VB}}\rangle$, respectively. Here, we assume that we have one *s*-like conduction band. According to the results in Ref. 34, the values of $|\langle S|p_\alpha|\alpha\rangle|^2$ with $\alpha\in\{X,Y,Z\}$ are taken to be equal. Consequently, the relative oscillator strength of the different transitions is then only proportional to the relative contributions of the valence $|X\rangle$-, $|Y\rangle$-, and $|Z\rangle$-like states. For the local strain in the *c*-plane system we assume the following:

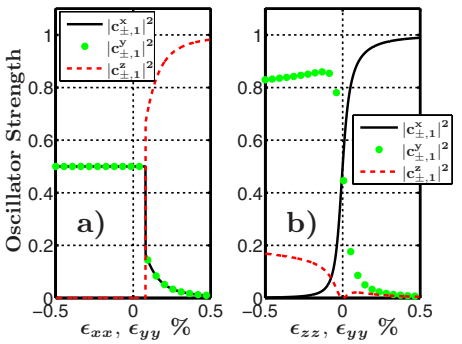

FIG. 3. (Color online) The relative oscillator strength of $|X\rangle$ ($|c^x_{\pm,1}|^2$), $|Y\rangle$ ($|c^y_{\pm,1}|^2$), and $|Z\rangle$ ($|c^z_{\pm,1}|^2$) components of the topmost valence-band transition in (a) c-plane and (b) a-plane GaN as a function of the strain.

$$\epsilon_{xx} = \epsilon_{yy}, \quad \epsilon_{zz} = -2\frac{C_{13}}{C_{33}}\epsilon_{xx}, \tag{11}$$

where the elastic constants are denoted by C_{ij}. The relative oscillator strength for the interband transition between the conduction band and the topmost valence band in a strained c-plane GaN system is shown in Fig. 3(a). From this we can conclude that the relative oscillator strength of $|X\rangle$- and $|Y\rangle$-like states is equal in the topmost valence band, and hence light emitted through the top surface will be isotropically polarized in the x-y plane. For compressive strain ($\epsilon_{xx}<0$), the topmost valence band is dominated by these contributions and has no $|Z\rangle$-like component for $\mathbf{k}=\mathbf{0}$. Under tensile strain, the relative oscillator strength of the top most valence band becomes predominantly $|Z\rangle$-like, which is characteristic of the crystal-field split-off band.

For the local strain in the a-plane system we apply[8]

$$\epsilon_{xx} = -\frac{C_{12}}{C_{11}}\epsilon_{yy} - \frac{C_{13}}{C_{11}}\epsilon_{zz}. \tag{12}$$

For the sake of a simplified discussion we assume here a biaxial strain ($\epsilon_{yy}=\epsilon_{zz}$). This ansatz is already sufficient to study the influence of anisotropic strain in the c plane (x-y plane). Due to the anisotropic strain in the c plane, we expect that the changes in the relative oscillator strength are very different from those in a c-plane system. The relative oscillator strength for the topmost valence band is shown in Fig. 3(b). In contrast to the c-plane system where one observes a superposition of $|X\rangle$- and $|Y\rangle$-like contributions, the a-plane system exhibits a strong difference between $|X\rangle$- and $|Y\rangle$-like oscillator strengths. Figure 3(b) shows that light emission arising from the $|Y\rangle$ state would increase more rapidly with compressive strain ($\epsilon_{yy}<0$) than that contributed by the $|Z\rangle$-like state. Thus, since the topmost valence band in an a-plane system is dominated by the $|Y\rangle$-like state, it is expected that the system exhibits nearly linearly polarized emission, for optical emission perpendicular to the top surface. This point is consistent with the experimental findings shown in Fig. 4, which displays the $T=6$ K near band-edge polarized PL spectra of the a-plane template that was characterized by HRXRD. Although the material is anisotropically strained in the y-z plane, if we take an average value for the strain, i.e., assume $\epsilon_{yy}=\epsilon_{zz}=-0.075\%$, it is evident that the relative oscillator strength predicted in Fig. 3(b) agrees well with the degree of anisotropy observed experimentally ($\sim 1:8$). We note that at the temperature used for the optical measurements, there will be a negligible thermal population of holes occupying the higher lying valence states and so it is reasonable to assume that the degree of anisotropy observed experimentally will reflect the wave-function character of only the topmost valence-band state. The linearly polarized emission of these systems is of significant potential benefit for a range of applications. For instance, by using light-emitting diodes which emit polarized light, the efficiency of liquid crystal displays could be dramatically increased.[35]

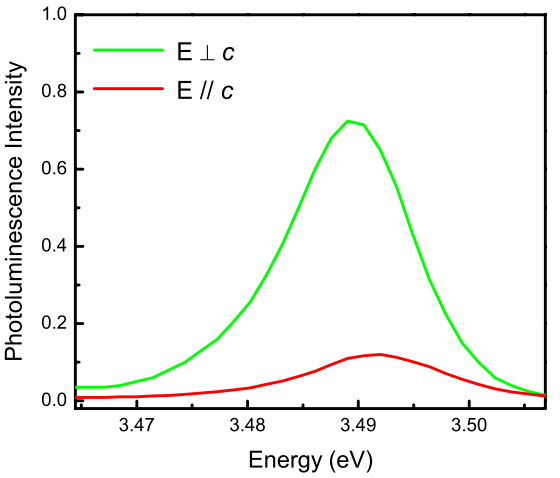

FIG. 4. (Color online) Polarised PL spectra covering the near band-edge region of the template measured at a temperature of $T=6$ K.

B. a-plane quantum well

As detailed in Sec. III A, the anisotropic strain within the a plane lowers the crystal symmetry from C_{6v} to C_{2v}, and therefore lifts the degeneracy of the $|X\rangle$-, $|Y\rangle$- and $|Z\rangle$-like valence-band states [cf. Fig. 2(b)]. To calculate the single-particle states in an a-plane GaN/$Al_{0.18}Ga_{0.82}N$ QW system we proceed in the following way. We assume that the QW is grown along the x direction. Since GaN is a direct band-gap material, it can be expected that excitonic transitions in a-plane GaN/AlGaN QWs involve mainly band-edge states with $\mathbf{k}_\parallel=(k_y,k_z)^T\approx\mathbf{0}$. According to Eq. (2), band-mixing effects will be of minor importance for these states, arising only from the weak spin-orbit interaction. To study the influence of this contribution on the single-particle energies and states separately from the effects arising from strain and quantum confinement, we neglect the spin-orbit contribution at first. With this approach, we can now study the single-particle states and energies in an a-plane GaN/$Al_{0.18}Ga_{0.82}N$ QW system by means of an effective-mass approximation. This approach should already be sufficient to investigate the influence of confinement and strain effects on the topmost $|X\rangle$-, $|Y\rangle$-, and $|Z\rangle$-like band-edge states. The effective masses along different directions are obtained from the Hamiltonian H_{kp} given in Eq. (4). Using the material parameters listed in

TABLE I. Material parameters for AlN and GaN. If not indicated otherwise all parameters are taken from Ref. 31.

	AlN	GaN
Δ_{so} (eV)	0.019	0.017
Δ_{cf} (eV)	−0.169	0.010
m_e (m_0)	0.329[a]	0.209[a]
A_1	−3.991[a]	−5.947[a]
A_2	−0.311[a]	−0.528[a]
A_3	3.671[a]	5.414[a]
A_4	−1.147[a]	−2.512[a]
A_5	−1.329[a]	−2.510[a]
A_6	−1.952[a]	−3.202[a]
a_1 (eV)	−4.08[b]	−4.08[b]
a_2 (eV)	−4.08[b]	−4.08[b]
(a_1-D_1) (eV)	−4.31[c]	−5.81[c]
(a_2-D_2) (eV)	−12.11[c]	−8.92[c]
D_3 (eV)	9.12[c]	5.47[c]
D_4 (eV)	−3.79[c]	−2.98[c]
D_5 (eV)	−3.23[c]	−2.82[c]
C_{11} (GPa)	396	390
C_{12} (GPa)	137	145
C_{13} (GPa)	108	106
C_{33} (GPa)	373	398
α (meV/K)	1.799	0.909
β (K)	1462	830

[a]Reference 29.
[b]Reference 23.
[c]Reference 36.

Table I, the resultant GaN relative effective mass values are given in Table II. Whilst the $|X\rangle$-like state has a light effective mass along the x direction, and the $|Y\rangle$- and $|Z\rangle$-like states have a heavy mass along this direction. Furthermore, the calculated effective masses of the $|Y\rangle$- and $|Z\rangle$-like states are almost equal along the x direction and therefore the influence of quantum confinement along this direction on these states will be nearly the same. The QW single-particle states

TABLE II. Relative effective masses of the $|X\rangle$, $|Y\rangle$, and $|Z\rangle$ valence bands (VB) along x, y and z (c) directions. The explicit numbers for the inverse effective masses in GaN are given in the lower half of the table using the parameters from Ref. 29.

VB	m^x/m_0	m^y/m_0	m^z/m_0
$\|X\rangle$	$1/(A_2+A_4+A_5)$	$1/(A_2+A_4-A_5)$	$1/(A_1+A_3)$
$\|Y\rangle$	$1/(A_2+A_4-A_5)$	$1/(A_2+A_4+A_5)$	$1/(A_1+A_3)$
$\|Z\rangle$	$1/A_2$	$1/A_2$	$1/A_1$
	Using the data from Ref. 29		
$\|X\rangle$	−0.180	−1.887	−1.876
$\|Y\rangle$	−1.887	−0.180	−1.876
$\|Z\rangle$	−1.894	−1.894	−0.1682

and energies are obtained by solving the one-dimensional Schrödinger equation

$$\left[-\frac{\hbar^2}{2}\frac{\partial}{\partial x}\frac{1}{m_{\alpha_i}^{\lambda,x}(E_{\alpha_i}^{\lambda})}\frac{\partial}{\partial x}+U_{\alpha}^{\lambda}(x)\right]\phi_{\alpha_i}^{\lambda}(x)=E_{\alpha_i}^{\lambda}\phi_{\alpha_i}^{\lambda}(x), \tag{13}$$

where the potential

$$U_{\alpha}^{\lambda}(x)=U_{\alpha}^{0,\lambda}(x)+S_{\alpha}^{\lambda}(x), \tag{14}$$

consists of the bare confinement potential in the x direction, $U_{\alpha}^{0,\lambda}(x)$, as well as a strain-dependent part, $S_{\alpha}^{\lambda}(x)$, with the index $\lambda=e,h$ for electrons and holes. The index α indicates $|S\rangle$-, $|X\rangle$-, $|Y\rangle$-, and $|Z\rangle$-like states. The conduction-band nonparabolicity is accounted for by allowing the effective mass to have an energy dependence,

$$\frac{1}{m_{S_i}^{e,x}(E_{S_i}^{e})}=\frac{1}{m_{S_i}^{e,x}(0)}[1-\beta(E_{S_i}^{e}-U_{S}^{e}(x))], \tag{15}$$

where the parameter β is given by[37]

$$\beta=\frac{1}{E_g}\left[1-\frac{m_{\alpha_i}^{\lambda,x}(0)}{m_0}\right]^2. \tag{16}$$

E_g denotes the semiconductor energy gap. More details on the numerical solution of Eq. (13) are given in the Appendix. In the case of the electron states we assume only an $|S\rangle$-like basis state S_{α}^{e} for which the strain-dependent term S_{α}^{e} can then be expressed as[38]

$$S^{e}=a_1\epsilon_{zz}+a_2(\epsilon_{xx}+\epsilon_{yy}). \tag{17}$$

Here, a_1 and a_2 denote the conduction-band deformation potentials. For the hole states the terms $S_{\alpha}^{\lambda}(x)$ are defined in Eqs. (8)–(10) for $|X\rangle$-, $|Y\rangle$-, and $|Z\rangle$-like states. The diagonal terms of the strain tensor ϵ_{ii} are determined from the XRD data discussed in Sec. II. Here, we have to take in principle into account that the XRD analysis was performed at room temperature while the PLE measurements were carried out at 6 K. Therefore, the lattice parameters would be expected to change slightly as a function of temperature. The anisotropy at 6 K should therefore be greater than that at 300 K, as there is a greater difference between the lattice parameters at 6 K (compared to growth temperature) than at 300 K (compared to growth temperature). However, we expect that the error associated with using the room-temperature strain values to be not much greater than the overall uncertainties associated with the x-ray analysis and therefore to have minimal impact on the calculated energy levels.

According to the experimental findings we consider $GaN/Al_{0.18}Ga_{82}N$ QWs using the material parameters listed in Table I. For the barrier material we use a linear interpolation to obtain all parameters except for the band gap where we apply $E_g^{Al_{0.18}Ga_{0.82}N}=3.85$ eV based on the experimental data given in Ref. 17. The bulk energy gap E_g^{GaN} of GaN (at zero temperature) is chosen to fit the calculated excitonic ground-state energy in the a-plane $GaN/Al_{0.18}Ga_{0.82}N$ QWs to the experimental data. The PLE experiments are performed at 6 K, for which the energy gap using the Varshni formula[31]

$$E_g^{\mathrm{GaN}}(T) = E_g^{\mathrm{GaN}}(T=0\ \mathrm{K}) - \frac{\alpha T^2}{T+\beta} \tag{18}$$

can be assumed identical to the 0 K values. The parameters α and β are given in Table I. We find that $E_g^{\mathrm{GaN}}(T=0\ \mathrm{K}) = 3.525$ eV gives the best fit to the full range of experimental data. This value is close to the recommended energy gap of 3.51 eV (at zero temperature) by Vurgaftman and Meyer.[31] Additionally, for electronic-structure calculations of QW or QD systems, one has to introduce the conduction-band ΔE_C and valence-band offset ΔE_V, which enter Eq. (13) via $U_\alpha^{0,\lambda}(x)$. The discussion of ΔE_V and the conduction-band to valence-band offset ratio given by Vurgaftman and Meyer in Ref. 31 is restricted to polar c-plane systems. To the best of our knowledge there are no calculations or measurements of the valence-band ΔE_V or conduction-band offset ΔE_C in the case of a nonpolar system. Here, we treat the conduction-band offset as a free parameter. The valence-band offset ΔE_V is then determined by the gap energy difference between bulk GaN and the barrier material. Doing so, one is able to give a first estimate of the conduction-band to valence-band offset ratio in a nonpolar GaN/AlGaN system. It is worth noting that ΔE_C and the electron effective mass cannot be determined independently. Since the effective electron masses observed in the literature scatter around $m_e=0.2m_0$ (Ref. 31) and to use a consistent set of parameters for the electron and hole masses around the Γ point, we apply a value of $m_e=0.209m_0$, taken from Ref. 29. Therefore, we are left with one primary adjustable parameter in our model, the conduction-band offset ΔE_C. As discussed, for example, in Ref. 39, the conduction-band offset ΔE_C can be determined if more than one QW-related transition is observed, by comparison between the experimental data and a series of theoretical calculations performed for different values of ΔE_C. Since the optical spectra discussed in Sec. IV exhibit more than one QW-related transition, this approach enables us to give an estimate of the conduction-band offset ΔE_C, and therefore also an estimate for the conduction-band to valence-band offset ratio $\Delta E_C:\Delta E_V$. Our analysis suggests a conduction-band to valence-band offset ratio of $\Delta E_C:\Delta E_V \approx 45:55$.

We also introduce the SO coupling into our calculations. The SO coupling is included as outlined by Chadi in Ref. 27 and discussed in more detail in Ref. 28. In this approach, the SO interaction acts on the basis states like the atomic SO operator on atomic orbitals. Here we take only $|Y_l\rangle$-like $[\phi_{Y_l}^h(x)]$ and $|Z_l\rangle$-like $[\phi_{Z_l}^h(x)]$ states into account since the energetic separation ϵ_l between these states is relatively small while the $|X_l\rangle$-like $[\phi_{X_l}^h(x)]$ states are clearly separated from the $|Y_l\rangle$- and $|Z_l\rangle$-like states due to quantum confinement and strain effects. The relevant SO-coupling matrix element is therefore given by $\langle Y_l\pm|H_{\mathrm{so}}|Z_l\mp\rangle = -i\lambda$ and its complex conjugate. According to Eq. (5), the parameter λ is given by $\lambda=\Delta_{\mathrm{so}}/3$. To achieve a compact notation, we denote the state $|\uparrow\rangle$ and $|\downarrow\rangle$ by $|+\rangle$ and $|-\rangle$, respectively. Hence, the Hamiltonian matrix H_{so}^l for the lth $|Y_l\rangle$- and $|Z_l\rangle$-like states reads

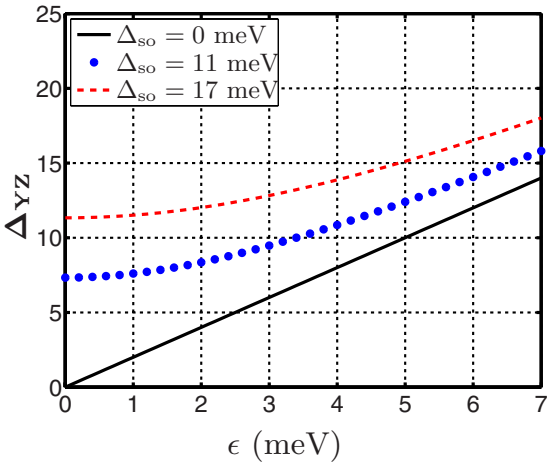

FIG. 5. (Color online) Splitting Δ_{YZ} between hole ground state and first excited hole hole state as a function of ϵ which is related to strain and confinement effects. Additionally, the influence of the spin-orbit coupling on the splitting Δ_{YZ} is shown for different values of the spin-orbit energy Δ_{so}.

$$H_{\mathrm{so}}^l = \begin{pmatrix} & |Y_l\pm\rangle & |Z_l\mp\rangle \\ \hline \langle Y_l\pm| & E_l^{\mathrm{AV}} + \epsilon_l & -i\lambda \\ \langle Z_l\mp| & i\lambda & E_l^{\mathrm{AV}} - \epsilon_l \end{pmatrix}, \tag{19}$$

where E_l^{AV} is the averaged energy of the lth $|Y_l\pm\rangle$- and $|Z\pm\rangle$-like states. ϵ_l describes the splitting between these states introduced by (i) the crystal-field splitting; (ii) the difference between S_y and S_z in Eqs. (9) and (10), and (iii) any small contribution due to differences in quantum confinement effects in the QW. The modified eigenenergies including the SO splitting are then given by

$$E_{Y_l}^{\mathrm{so}} = \frac{1}{2}(E_{Y_l} + E_{Z_l}) + \sqrt{\lambda^2 + \epsilon_l^2}, \tag{20}$$

$$E_{Z_l}^{\mathrm{so}} = \frac{1}{2}(E_{Y_l} + E_{Z_l}) - \sqrt{\lambda^2 + \epsilon_l^2}. \tag{21}$$

The influence of the SO coupling on the splitting $\Delta_{YZ}=E_{Y_1}^{\mathrm{so}}-E_{Z_1}^{\mathrm{so}}$ between the hole ground state $\phi_{Y_1}^h(x)$ and the first excited state $\phi_{Z_1}^h(x)$ is shown in Fig. 5 as a function of $\epsilon_{l=1}$ and for different values of Δ_{so}. Since in the following we are discussing the splitting between the first two hole states only, we drop the index l. Without the spin-orbit coupling (solid line) the splitting Δ_{YZ} is then given by 2ϵ. For larger values of ϵ the splitting Δ_{YZ} is only slightly modified by the SO coupling while for small values of ϵ, Δ_{YZ} is dominated by the SO coupling. Additionally, from this analysis we can conclude that if the energetic separation of the different single-particle states is large compared to the SO coupling term λ, the influence of this contribution is of minor importance. Therefore, our approach to take the SO coupling into account between $|Y\rangle$- and $|Z\rangle$-like states only is well justified.

The corresponding eigenstates $\mathbf{u}_{Y_l,Z_l}=(u_Y^l, u_Z^l)^T$ can be obtained from

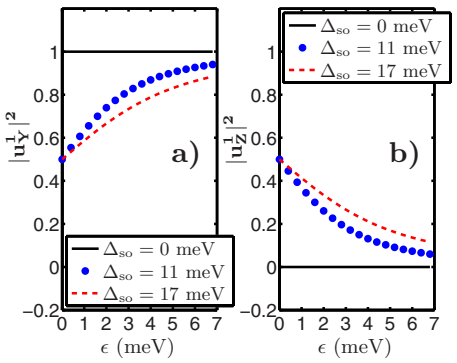

FIG. 6. (Color online) The squared (a) $|Y\rangle$-like ($|u_Y^1|^2$) and (b) $|Z\rangle$-like ($|u_Z^1|^2$) contributions to the hole ground state as function of ϵ, which describes the splitting between hole ground state and first excited state due to strain and confinement effects. The influence of spin-orbit splitting energy Δ_{so} is studied separately.

$$\left| \begin{array}{l} (E_l^{AV} + \epsilon_l - E_{Y_l,Z_l}^{so})u_Y^l - i\lambda u_Z^l = 0 \\ i\lambda u_Y^l + (E_l^{AV} - \epsilon_l - E_{Y_l,Z_l}^{so})u_Z^l = 0 \end{array} \right| . \tag{22}$$

The components u_Y^1 and u_Z^1 of the hole ground state can be written in the following form:

$$u_Y^1 = \sqrt{\frac{1+\alpha}{2}}, \quad u_Z^1 = i\sqrt{\frac{1-\alpha}{2}}, \tag{23}$$

where α reads

$$\alpha = \frac{\epsilon}{\sqrt{\epsilon^2 + \lambda^2}}. \tag{24}$$

To analyze the influence of the SO coupling on the single-particle states, Figs. 6(a) and 6(b) show the relative contributions of the $|Y\rangle$- and $|Z\rangle$-like states, respectively, to the hole ground state as a function of ϵ. In the absence of the SO interaction, the ground-state hole wave function is purely $|Y\rangle$ like since $|u_Y^1|^2=1$ and $|u_Z^1|^2=0$ independent of ϵ. In the presence of the SO coupling ($\lambda \neq 0$) we observe a mixing of the $|Y\rangle$- and $|Z\rangle$-like components. This mixing is tightly linked to the energetic splitting ϵ of the ground state and the first excited state: with $\epsilon=0$ the hole ground state $\phi_{Y_1}^h(x)$ and the first excited hole state $\phi_{Z_1}^h(x)$ are degenerate in the absence of the SO coupling. Therefore, the splitting between the ground state and first excited state is determined by the SO coupling in the case of $\epsilon=0$ [cf. Eq. (19); cf. Fig. 5], and the fraction of $|Y\rangle$- and $|Z\rangle$-like components to the ground state is equal ($|u_Y^1|^2=0.5$, $|u_Z^1|^2=0.5$; cf. Fig. 6). With increasing ϵ the influence of the SO coupling on the mixing of the different valence-band states is reduced. For instance as depicted in Fig. 6(a), with $\Delta_{so}=17$ meV (dashed red line), the contribution from the $|Z\rangle$-like state to hole ground state $\phi_{Y_1}^h(x)$ varies from 50% ($\epsilon=0$ meV) to 11% ($\epsilon=7$ meV). This behavior is only slightly modified when changing Δ_{so} from 17 to 11 meV (blue dotted line). However, this analysis reveals that even though the SO splitting is relatively weak in GaN compared, for example, to InAs ($\Delta_{so}=390$ meV),[40] it can still have a considerable influence on the intermixing of the different valence-band states in the highest hole states.

To compare the theoretical results with PLE data from different a-plane GaN QWs, we have to calculate the excitonic transition energies as a function of the QW width L_w. Here, the transition energies are calculated according to

$$E_{i,j}^X = E_g^{GaN} + E_i^e - E_j^h - E_X^b. \tag{25}$$

The electron and hole single-particle energies calculated from Eqs. (13) and (19) are denoted by E_i^e and E_j^h, respectively. E_X^b refers to the excitonic binding energy. For a realistic treatment of the excitonic binding energy E_b in a QW system neither a two-dimensional model nor a three-dimensional model is suitable since the motion of the carriers is somewhere in between these two limiting cases. Therefore, we apply the approach developed in Refs. 19 and 41 using a fractional-dimensional space. Doing so, the excitonic problem in αD space in a QW reduces to the one of an hydrogenlike atom. More details on these calculations are given in Ref. 20.

IV. PLE SPECTROSCOPY AND COMPARISON WITH THEORY

For the optical measurements, the samples were mounted on the finger of a variable temperature closed cycle He cryostat. Light from a 300 W Xenon lamp, dispersed by a 0.25 m spectrometer, was used to provide a tunable wavelength excitation source for the PLE measurements. The luminescence was focused into a 0.85 m double grating spectrometer and detected by a Peltier-cooled GaAs photomultiplier tube, and then processed using standard lock-in techniques. For the polarization-dependent PLE studies, a Nicol prism was used to select the appropriate plane of linearly polarized excitation light in the backscattering geometry $k \perp c$ where c is the polar axis of the samples. The PLE spectra have been corrected for the spectral response of the Xenon lamp and the 0.25 m spectrometer. The numerical values quoted for the features in the PLE spectra were obtained by measuring the wavelength of the scattered light using the double spectrometer.

We now discuss the low-temperature PLE spectroscopy of the nonpolar a-plane GaN/AlGaN multiple QW structures. Shown in Fig. 7 are PLE spectra of the five QW samples, containing GaN QWs of thicknesses ranging from 24 to 72 Å. For each structure the excitation spectrum is detected on the low-energy side of the photoluminescence emission peak.[17] The ground-state ($n=1$) exciton, associated with the creation of excitons bound to the $n=1$ electron subband, is clearly resolved as the lowest energy peak in each of the spectra and is seen to redshift with increasing QW width. In structures with QWs wider than 24 Å, another higher energy excitonic feature is observed with an energy separation from the $n=1$ exciton that decreases with increasing QW width. We assign this feature to the creation of excitons bound to the $n=2$ electron subband. However, when linearly polarized excitation is used ($E \perp c, E \| c$), both of the exciton transitions observed with unpolarized light are shown to consist of two overlapping peaks, which we attributed previously to transitions involving different valence subbands.[42] The polarized

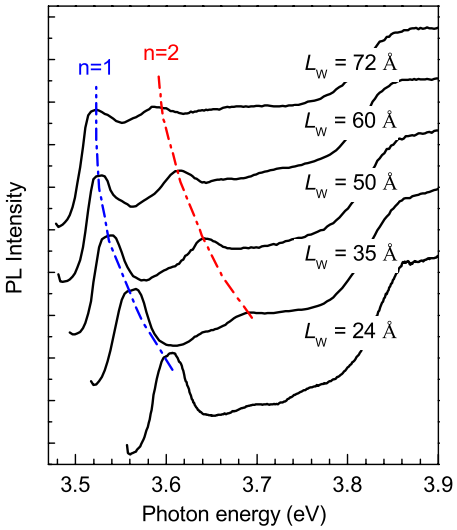

FIG. 7. (Color online) PLE spectra of the series of QW structures, measured using unpolarised light at a temperature of 6 K. Excitonic transitions involving $n=1$ and $n=2$ subbands are indicated in the figure.

PLE spectra for the 50 Å QW are shown in Fig. 8. For the transitions associated with the $n=1$ electron subband, the peaks occur at 3.540 and 3.557 eV; for those associated with the $n=2$ electron subband, the peaks are at 3.644 and 3.657 eV. The same general behavior was observed in the PLE spectra for all samples in the series. Also observed in Fig. 8, between 3.58 and 3.60 eV for the $E\perp c$, $E\|c$ polarized light, respectively, is a feature which we have assigned to the onset of the $n=1$ continuum.[42]

This analysis of the excitonic transitions is supported by the calculated single-particle states and the subsequently evaluated transition energies. A schematic illustration of the electronic structure of the 50 Å QW is displayed in Fig. 9. According to Table II, the $|X\rangle$-like state has a light-hole mass along the growth direction (x direction) while the $|Y\rangle$- and $|Z\rangle$-like states have heavy masses along the growth direction.

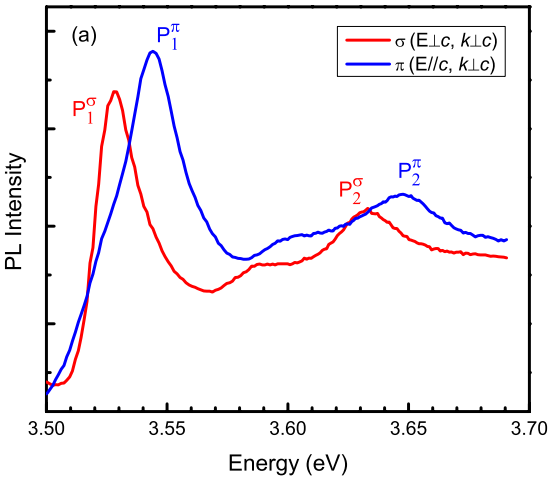

FIG. 8. (Color online) Polarized PLE spectra of the 50 Å QW structure, with the wave vector **k** of the exciting light parallel to the growth direction (x direction).

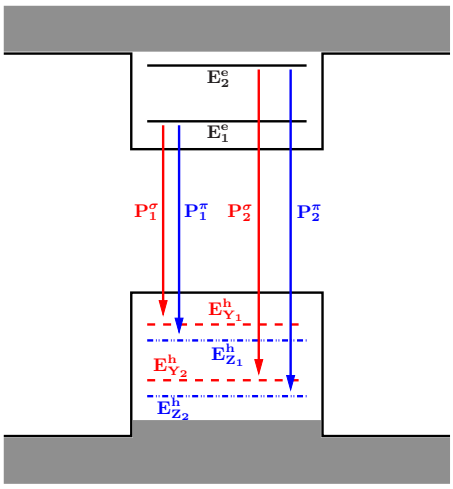

FIG. 9. (Color online) Schematic illustration of the electronic structure of an 50 Å a-plane GaN QW. The transitions between the electron states and the hole levels are indicated by the vertical lines. Here, we use the notation introduced in Sec. IV. The gray-shaded area denotes energetically higher lying states.

Here, the hole ground state is a $|Y\rangle$-like state $[\phi_{Y_1}^h(x)]$ while the first excited state is a $|Z\rangle$-like state $[\phi_{Z_1}^h(x)]$. The second and third excited hole states are $|Y\rangle$-like $[\phi_{Y_2}^h(x)]$ and $|Z\rangle$-like $[\phi_{Z_2}^h(x)]$ states, respectively. According to the analysis of the bulk system, the peaks P_1^σ and P_1^π can be attributed to a transition from the $\phi_{Y_1}^h(x)$ and $\phi_{Z_1}^h(x)$ hole states, respectively, to the electron ground state $\phi_1^e(x)$ (cf. Fig. 9). Likewise, the peaks labeled P_2^σ and P_2^π in Fig. 8 are attributed to transitions from holes in the second $\phi_{Y_2}^h(x)$ and third $\phi_{Z_2}^h(x)$ excited states, respectively, to the first excited electron state $\phi_2^e(x)$ $(n=2)$.

Based on the results for the single-particle energies including strain effects, SO coupling and nonparabolicity contributions we calculate the energetic position of the $P_1^{\sigma,\pi}$ and $P_2^{\sigma,\pi}$ peaks as a function of the QW width according to Eq. (25). Importantly, the influence of the SO coupling on the polarization properties of the exciton transitions, as discussed in Sec. III B, is also revealed in the PLE spectra: the pronounced low-energy shoulder on the P_1^π peak shown in Fig. 8 is evidence of the band mixing between $|Y\rangle$- and $|Z\rangle$-like states for the ground-state transition. The same behavior is seen for all QW widths, but is particularly clear in the 35 A QW structure, as is shown in Fig. 10.

The energies of the σ and π polarized transitions are averaged for the $n=1$ and $n=2$ subbands and are denoted in the following by P_1 and P_2, respectively. For the exciton transitions associated with the $n=1$ electron state the values for the calculated exciton binding energy E_b were found to lie in the range of ≈32 to ≈26 meV for 24 to 72 Å wide QWs. The theoretical results and the experimental data for P_1, P_2, and the energetic separation $\Delta_{1,2}=P_2-P_1$ are shown in Figs. 11–13, respectively. We consider here three different band offset ratios, $\Delta E_C:\Delta E_V=25:75$ (dashed line), $\Delta E_C:\Delta E_V=45:55$ (solid line), and $\Delta E_C:\Delta E_V=65:35$ (dashed-dotted line). As we will show in the following, the best agreement for P_1, P_2, and $\Delta_{1,2}=P_2-P_1$ is obtained for the $\Delta E_C:\Delta E_V=45:55$ offset.

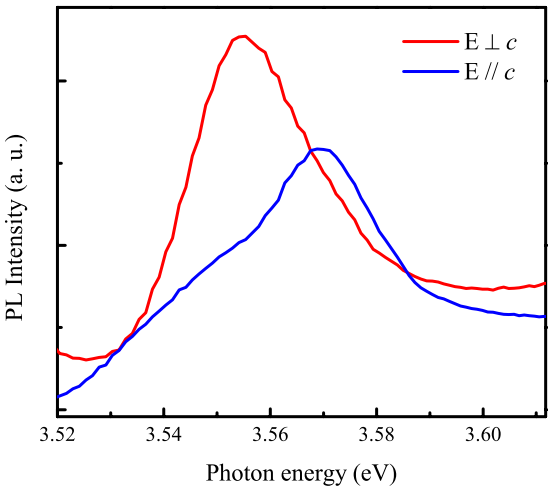

FIG. 10. (Color online) Polarized PLE spectra of the 35 Å QW structure measured at a temperature of $T=6$ K.

Looking at P_1 shown in Fig. 11, a very good agreement between experiment and theory is observed when using $\Delta E_C:\Delta E_V=65:35$. However, for $L_w>30$ Å we also find that the transitions energies for $\Delta E_C:\Delta E_V=45:55$ agree within ≈ 6 meV. It should be mentioned at this point that the QW width values have been determined previously by XRD,[17] however a subsequent transmission electron microscopy investigation of the 72 Å structure has revealed that there is a ± 6 Å (~ 2 ML) width fluctuation of both the barriers and QWs throughout the stack. Although this thickness variation is very reasonable, considering the relatively low crystalline quality of the *a*-plane template, it necessarily reduces the degree of certainty able to be achieved in the comparison of the theoretical and experimental values. While the influence of the well width fluctuations on the single-particle states become less important for the thicker QWs ($L_w>30$ Å) it will become more important for the transition energies of the thinner QW structures ($L_w \leq 30$ Å). Therefore, the discrepancy between theory and experiment observed especially for the well width $L_w=24$ Å might arise from the well width fluctuations. However, since the transmission electron microscopy results are available for the 72 Å structure only, and the theoretical results are in very good agreement with the experimental results for the thicker QWs, we proceed with the QW width values obtained in Ref. 17 by XRD measurements.

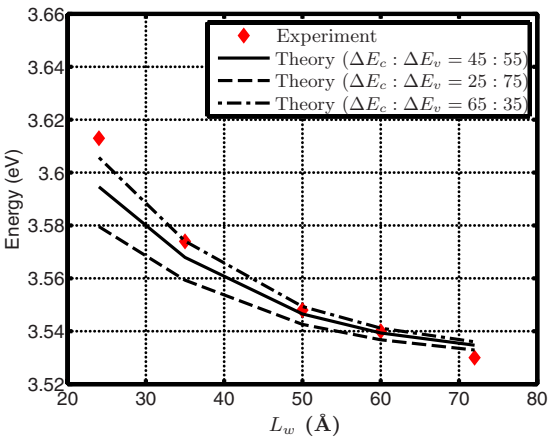

FIG. 11. (Color online) Energetic position of the low-energy peak P_1 as a function of the QW width. The energies of the σ and π polarized transitions P_1^σ and P_1^π, shown in Fig. 8, are averaged.

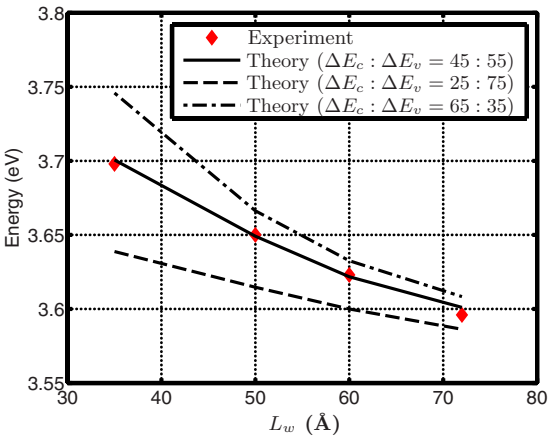

FIG. 12. (Color online) Energetic position of the high-energy peak P_2 as a function of the QW width L_w. The energies of the σ- and π-polarized transitions P_2^σ and P_2^π, shown in Fig. 8, are averaged.

As disccussed by Duggan[43] in detail, the ground-state transition in QW structure shows only a weak dependence on the band offset ratio. Therefore, the comparison of the theoretical results and the experimental data for P_1 on its own is not sufficient to determine the band offset ratio. The sensitivity on this quantity is increased by studying transitions between excited electron and hole states.

The peaks $P_2^{\sigma,\pi}$ shown in Fig. 8 involve the first excited electron state ϕ_2^e ($n=2$). For the transitions associated with this electron state, we have approximated the excitonic binding energy in the following way: due to the low effective electron mass, compared to the hole effective masses, the first excited electron state ϕ_2^e is not very strongly bound in the QW, especially for narrower well widths. Consequently, the electron wave functions spread considerably into the barrier material. Therefore, one could expect that the excitonic binding energy of the transitions associated with the $n=2$

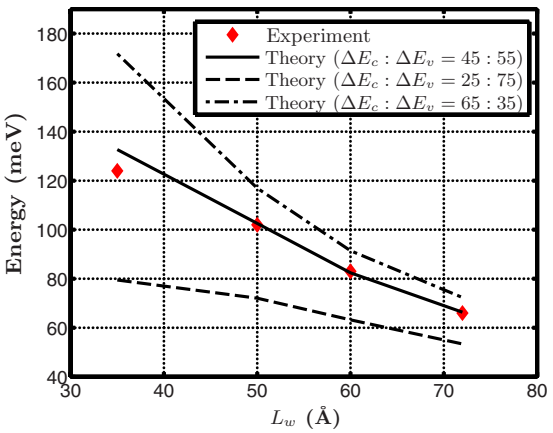

FIG. 13. (Color online) Calculated splitting $\Delta_{1,2}$ between the peaks P_1 and P_2 as a function of the QW width L_w.

electron state would be close to that of the binding energy in the bulk system of the barrier material. To obtain the exciton binding energy of the bulk barrier material we apply a linear interpolation between the bulk exciton binding energies of AlN and GaN. The measured bulk AlN excitonic binding energies scatter around 48 meV.[44–46] For GaN, values of 25–26 meV (Refs. 13, 47, and 48) are experimentally observed. The linear interpolation of these experimental values gives an excitonic binding of $E_b^{\mathrm{exp}} \approx 29$ meV for the $Al_{0.18}Ga_{0.82}N$ barrier material. When using the bulk GaN exciton binding energy determined from our model ($E_b \approx 20$ meV), we obtain a binding energy of $E_b \approx 25$ meV for the $Al_{0.18}Ga_{0.82}N$ barrier material. Since the transition energies $P_2^{\sigma,\pi}$ are on the order of a few electron volts, a difference of 4 meV between E_b^{exp} and E_b is only of minor importance for the theory experiment comparison of the P_2 transition energies. In the following we use $E_b = 25$ meV for the $Al_{0.18}Ga_{0.82}N$ barrier material.

By using a conduction-band to valence-band offset ratio of $\Delta E_C : \Delta E_V \approx 65:35$, the theoretical and experimental results for $L_w = 35$ Å differ by ≈ 50 meV while with $\Delta E_C : \Delta E_V \approx 45:55$ we find an excellent agreement between the theoretical results and the experimental data, as shown by the solid line in Fig. 12. As expected, the close agreement between the experimentally observed and theoretically predicted values of P_1 and P_2 shown in Figs. 11 and 12 is extended to the QW width dependence of their energetic separation $\Delta_{1,2} = P_2 - P_1$, as shown by the solid line in Fig. 13. Therefore, from this detailed analysis we can conclude that the band offset ratio $\Delta E_C : \Delta E_V \approx 45:55$ gives the most consistent agreement between the results presented in Figs. 11–13.

To gain further insight into the electronic structure of the *a*-plane GaN/$Al_{0.18}Ga_{0.82}N$ QWs, we now analyze the splitting $\Delta_1^{\sigma,\pi}$ between the two peaks associated with $n=1$ electron state (P_1^{σ} and P_1^{π}). A closer inspection of the PLE measurements reveals that the splitting $\Delta_1^{\sigma,\pi}$ between the two peaks P_1^{σ} and P_1^{π} is seen to be essentially independent of QW width L_w ($\sim 15 \pm 3$ meV) within the accuracy of the measurement (± 5 meV). The same is true for the energetic separation of the peaks P_2^{σ} and P_2^{π}. This behavior can be explained by looking at the effective masses of the $|Y\rangle$- and $|Z\rangle$-like hole states, given in Table II. Since the effective masses of the $|Y\rangle$- and $|Z\rangle$-like hole states are almost equal along the growth direction, the effect of the change in L_w and therefore in the confinement potential on the single-particle states will be very similar. The calculated splitting $\Delta_1^{\sigma,\pi}$ ($\Delta_2^{\sigma,\pi}$) is shown in Fig. 14 as a function of the QW width L_w. From this we can conclude that the variation in the splittings $\Delta_1^{\sigma,\pi}$ ($\Delta_2^{\sigma,\pi}$) for the P_1^{σ} (P_2^{σ}) and P_1^{π} (P_2^{π}) peaks is less than 0.5 meV and therefore is almost unaffected by the change in the QW width L_w. Furthermore, since the splittings $\Delta_i^{\sigma,\pi}$ are very sensitive to the values of the SO splitting energy Δ_{so} and the crystal-field splitting Δ_{cf}, our analysis of $\Delta_i^{\sigma,\pi}$ allows us to give further insight in the magnitude of these parameters. Of course the splittings $\Delta_i^{\sigma,\pi}$ also depend on the strain state of the system. To study the influence of the strain on the splittings $\Delta_i^{\sigma,\pi}$ we have artificially switched off crystal-field and SO splitting. Since $\epsilon_{zz} = -0.05$ and $\epsilon_{yy} = -0.1$ are relatively small, the splitting introduced by the strain is only on the order of 3 meV, and yields therefore only a small contribution to $\Delta_1^{\sigma,\pi}$ and $\Delta_2^{\sigma,\pi}$. So far we have used $\Delta_{\mathrm{so}} = 17$ meV and $\Delta_{\mathrm{cf}} = 10$ meV as recommended by Vurgaftman and Meyer.[31] However, the SO splitting energies Δ_{so} in wurtzite GaN discussed by Vurgaftman and Meyer[31] range from 11 to 20 meV. The values for the crystal-field splitting Δ_{cf} in GaN scatter between 9 and 42 meV.[31] A recent first-principle calculation of Δ_{cf} gave a value of $\Delta_{\mathrm{cf}} = 33$ meV.[29] From our analysis in Sec. III B, one finds that for the smallest spin-orbit coupling of $\Delta_{\mathrm{so}} = 11$ meV reported in Ref. 31, the crystal-field splitting Δ_{cf} has than to be in the region of 10–18 meV to match the experimental data. Therefore, our investigation in comparison with the experimental data supports the recommended values of Vurgaftman and Meyer[31] for crystal-field splitting and SO coupling energies.

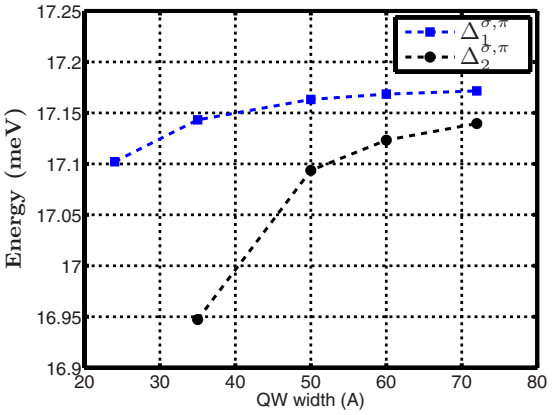

FIG. 14. (Color online) Calculated splitting $\Delta_1^{\sigma,\pi}$ ($\Delta_2^{\sigma,\pi}$) between the peaks P_1^{σ} (P_2^{σ}) and P_1^{π} (P_2^{π}) as a function of the QW width.

V. CONCLUSION

In conclusion, we have performed a comprehensive characterization of the optical properties of a series of nonpolar GaN/AlGaN QWs, grown on *a*-plane GaN templates, using HRXRD, excitation spectroscopy, and $\mathbf{k}\cdot\mathbf{p}$ theory. From the HRXRD data, the in-plane strain state of the film was determined to be compressive and anisotropic. With this information, the band structure and polarization properties of bulk *a*-plane material was then calculated using a $\mathbf{k}\cdot\mathbf{p}$-based theory. The anisotropic strain in the basal (c) plane is shown to result in a lifting of the degeneracy of the $|X\rangle$- and $|Y\rangle$-like valence bands. Here, we find that the lowest energy valence band, including quantum confinement effects, is predominantly $|Y\rangle$-like and the next lowest is $|Z\rangle$-like. The relative oscillator strength of the lowest energy transition was also determined and compared to the polarization ratio of low-temperature PL data, where close agreement was seen. The single-particle state energies were then determined as a function of QW width and successfully compared with the results of polarized excitation spectroscopy. The observation of exciton transitions bound to the $n=2$ subband allowed an estimate of the conduction to valence-band offset ratio to be made, which was found to be $\approx 45:55$. Due to the similarity of the effective masses of the $|Y\rangle$- and $|Z\rangle$-like states, the

valence subband structure of the QWs was shown to be approximately independent of QW width over the range of widths investigated. From this analysis we were also able to gain further insight in the magnitude of the crystal-field splitting and SO coupling energies. Our theoretical results in comparison with the experiments of the valence subband structure indicates values for the SO coupling and the crystal-field splitting energies which are close to the values recommended by Vurgaftman and Meyer.[31] The effect of valence-band mixing induced by spin-orbit coupling is also studied and qualitatively verified on the basis of comparisons with the spectral form of the exciton peaks.

ACKNOWLEDGMENTS

This work was carried out with the financial support of the United Kingdom Engineering and Physical Sciences Research Council under Grants No. EP/EC35167/1 and No. EP/E035191/1. E.P.O. and S.S. acknowledge financial support from Science Foundation Ireland. S.S. was further supported by the Irish Research Council for Science, Engineering and Technology (IRCSET).

APPENDIX

Band nonparabolicity effects are accounted for in our approach by allowing the effective mass to have an energy dependence given by Eq. (15). As discussed by Harrison,[37] the Schrödinger equation given in Eq. (13) can be solved by using an iterative shooting method with the additional feature of adjusting the effective mass for each energy E. Here, we present a noniterative approach, based on the finite difference method. To begin with we neglect the energy dependence of the effective mass. In general the Schrödinger equation given in Eq. (13) is of the form

$$\left[-\frac{\hbar^2}{2}\frac{\partial}{\partial x}\frac{1}{m(x)}\frac{\partial}{\partial x}+U(x)\right]\phi(x)=E\phi(x). \tag{A1}$$

Using the finite-difference formulas given in Ref. 49, the differential operators can be written in matrix form (D). Therefore, the matrix representation of the Schrödinger equation is then given by

$$(D+U)\phi=E\phi. \tag{A2}$$

Doing so, we are left with the well-known eigenvalue problem. The new contribution is now the explicit inclusion of the nonparabolicity effects by taking into account the energy dependence of the effective mass. By using[50] $E=\frac{\hbar^2k^2}{2m(x)}(1-\beta k^2)$ and $1/m(x)=\frac{1}{\hbar^2}\frac{\partial^2E}{\partial k^2}$ the energy dependence of the effective mass reads

$$\frac{1}{m(E,x)}=\frac{1}{m(0,x)}[1-\beta(E-U(x))], \tag{A3}$$

where β is defined according to Eq. (16). By substituting this expression into Eq. (A1) and using again the finite-difference expression for the differential operators $A(x)\partial^2/\partial x^2$ and $B(x)\partial/\partial x$ given in Ref. 49, the matrix representation of the Schrödinger equation becomes

$$[D-ED(\beta)+D(U)+U]\phi=E\phi, \tag{A4}$$

where $D(\beta)$ and $D(U)$ take into account the position dependence of β and the confinement potential U, respectively. Therefore, we are left with

$$[D+D(U)+U]\phi=E(1+D(\beta))\phi$$

$$\Leftrightarrow[1+D(\beta)]^{-1}[D+D(U)+U]\phi=E\phi. \tag{A5}$$

Here, the single-particle states and energies are obtained from the eigenvalue problem given by Eq. (A5).

[1] S. Nakamura, T. Mukai, and M. Senoh, Appl. Phys. Lett. **64**, 1687 (1994).
[2] S. Strite and H. Morkoc, J. Vac. Sci. Technol. B **10**, 1237 (1992).
[3] S. Nakamura, M. Senoh, N. Iwasa, and S. Nagahama, Jpn. J. Appl. Phys., Part 2 **34**, L797 (1995).
[4] T. Takeuchi, S. Sota, M. Katsuragawa, M. Komori, H. Takeuchi, H. Amano, and I. Akasaki, Jpn. J. Appl. Phys., Part 2 **36**, L382 (1997).
[5] J. S. Im, H. Kollmer, J. Off, A. Sohmer, F. Scholz, and A. Hangleiter, Phys. Rev. B **57**, R9435 (1998).
[6] P. Waltereit, O. Brandt, A. Trampert, H. T. Grahn, J. Menniger, M. Ramsteiner, and K. H. Ploog, Nature (London) **406**, 865 (2000).
[7] T. Paskova, Phys. Status Solidi B **245**, 1011 (2008).
[8] S. Schulz, A. Berube, and E. P. O'Reilly, Phys. Rev. B **79**, 081401(R) (2009).
[9] M. C. Schmidt, K. C. Kim, H. Sato, N. Fellows, H. Masui, S. Nakamura, S. P. DenBaars, and J. S. Speck, Jpn. J. Appl. Phys., Part 2 **46**, L126 (2007).
[10] M. C. Schmidt, K. C. Kim, R. M. Farrel, D. F. Feezell, D. A. Cohen, M. Saito, K. Fujito, J. S. Speck, S. P. DenBaars, and S. Nakamura, Jpn. J. Appl. Phys., Part 2 **46**, L190 (2007).
[11] K. Okamoto, T. Tanaka, M. Kubota, and H. Ohta, Jpn. J. Appl. Phys., Part 2 **46**, L820 (2007).
[12] T. Gühne, Z. Bougrioua, S. Laugt, M. Nemoz, P. Vennegues, B. Vinter, and M. Leroux, Phys. Rev. B **77**, 075308 (2008).
[13] A. Alemu, B. Gil, M. Julier, and S. Nakamura, Phys. Rev. B **57**, 3761 (1998).
[14] S. Ghosh, P. Waltereit, O. Brandt, H. T. Grahn, and K. H. Ploog, Phys. Rev. B **65**, 075202 (2002).
[15] S. Ghosh, P. Misra, H. T. Grahn, B. Imer, S. Nakamura, S. P. DenBaars, and J. S. Speck, J. Appl. Phys. **98**, 026105 (2005).
[16] S. Ghosh, P. Misra, H. T. Grahn, B. Imer, S. Nakamura, S. P. DenBaars, and J. S. Speck, Phys. Status Solidi B **243**, 1441 (2006).
[17] T. J. Badcock, P. Dawson, M. J. Kappers, C. McAleese, J. L. Hollander, C. F. Johnston, D. V. S. Rao, A. M. Sanchez, and C. J. Humphreys, Appl. Phys. Lett. **93**, 101901 (2008).
[18] M. A. Moram and M. E. Vickers, Rep. Prog. Phys. **72**, 036502

(2009).
[19] H. Mathieu, P. Lefebvre, and P. Christol, Phys. Rev. B **46**, 4092 (1992).
[20] S. Schulz and E. P. O'Reilly, Phys. Status Solidi C **7**, 1900 (2010).
[21] M. A. Moram, Z. H. Barber, and C. J. Humphreys, J. Appl. Phys. **102**, 023505 (2007).
[22] M. A. Moram, C. F. Johnston, J. L. Hollander, M. J. Kappers, and C. J. Humphreys, J. Appl. Phys. **105**, 113501 (2009).
[23] A. D. Andreev and E. P. O'Reilly, Phys. Rev. B **62**, 15851 (2000).
[24] S. Schulz, S. Schumacher, and G. Czycholl, Phys. Rev. B **73**, 245327 (2006).
[25] G. Bester and A. Zunger, Phys. Rev. B **71**, 045318 (2005).
[26] D. P. Williams, S. Schulz, A. D. Andreev, and E. P. O'Reilly, IEEE J. Sel. Top. Quantum Electron. **15**, 1092 (2009).
[27] D. J. Chadi, Phys. Rev. B **16**, 790 (1977).
[28] S. Schulz, S. Schumacher, and G. Czycholl, Eur. Phys. J. B **64**, 51 (2008).
[29] P. Rinke, M. Winkelnkemper, A. Qteish, D. Bimberg, J. Neugebauer, and M. Scheffler, Phys. Rev. B **77**, 075202 (2008).
[30] M. Murayama and T. Nakayama, Phys. Rev. B **49**, 4710 (1994).
[31] I. Vurgaftman and J. R. Meyer, J. Appl. Phys. **94**, 3675 (2003).
[32] B. Gil and A. Alemu, Phys. Rev. B **56**, 12446 (1997).
[33] R. Tao, T. Yu, C. Jia, Z. Chen, Z. Qin, and G. Zhang, Phys. Status Solidi A **206**, 206 (2009).
[34] M. Suzuki and T. Uenoyama, Jpn. J. Appl. Phys., Part 1 **35**, 543 (1996).
[35] H. Masui, M. Schmidt, N. Fellows, H. Yamada, K. Iso, J. S. Speck, S. Nakamura, and S. P. DenBaars, Phys. Status Solidi A **206**, 203 (2009).
[36] Q. Yan, P. Rinke, M. Scheffler, and C. G. Van de Walle, Appl. Phys. Lett. **95**, 121111 (2009).
[37] P. Harrison, *Quantum Wells, Wires and Dots: Theoretical and Computational Physics of Semiconductor Nanostructures* (Wiley, New York, 2005).
[38] S. L. Chuang, IEEE J. Quantum Electron. **32**, 1791 (1996).
[39] M. H. Meynadier, C. Delalande, G. Bastard, M. Voos, F. Alexandre, and J. L. Lievin, Phys. Rev. B **31**, 5539 (1985).
[40] I. Vurgaftman, J. R. Meyer, and L. R. Ram-Mohan, J. Appl. Phys. **89**, 5815 (2001).
[41] X. F. He, Phys. Rev. B **43**, 2063 (1991).
[42] T. J. Badcock, P. Dawson, M. J. Kappers, C. McAleese, J. L. Hollander, C. F. Johnston, D. V. S. Rao, A. M. Sanchez, and C. J. Humphreys, J. Appl. Phys. **105**, 123112 (2009).
[43] G. Duggan, J. Vac. Sci. Technol. B **3**, 1224 (1985).
[44] E. Silveira, J. A. J. Freitas, O. J. Glembocki, G. A. Slack, and L. J. Schowalter, Phys. Rev. B **71**, 041201(R) (2005).
[45] R. A. R. Leute, M. Feneberg, R. Sauer, K. Thonke, S. B. Thapa, F. Scholz, Y. Taniyasu, and M. Kasu, Appl. Phys. Lett. **95**, 031903 (2009).
[46] T. Onuma, T. Shibata, K. Kosaka, K. Asai, S. Sumiya, M. Tanaka, T. Sota, A. Uedono, and S. F. Chichibu, J. Appl. Phys. **105**, 023529 (2009).
[47] S. J. Xu, W. Liu, and K. F. Li, Appl. Phys. Lett. **81**, 2959 (2002).
[48] A. V. Rodina, M. Dietrich, A. Goldner, L. Eckey, A. Hoffmann, A. L. Efros, M. Rosen, and B. K. Meyer, Phys. Rev. B **64**, 115204 (2001).
[49] S. L. Chuang and C. S. Chang, Semicond. Sci. Technol. **12**, 252 (1997).
[50] D. F. Nelson, R. C. Miller, and D. A. Kleinman, Phys. Rev. B **35**, 7770 (1987).